METAMATERIALS-BY-DESIGN

Photonic Materials and Applications Series

Published in association with the SPIE, the international society for optics and photonics

Series Editor

Lorenzo Pavesi
University of Trento, Italy

Volumes in the series

Metal Halide Perovskites for Generation, Manipulation and Detection of Light
Edited by Juan P. Martínez-Pastor, Pablo Boix, Guichuan Xing

Metamaterials-by-Design
Edited by Andrea Alù, Nader Engheta, Andrea Massa, Giacomo Oliveri

Neuromorphic Photonic Devices and Applications
Edited by Min Gu, Elena Goi, Yangyundou Wang, Zhengfen Wan, Yibo Dong, Yuchao Zhang, Haoyi Yu

Biophotonics and Biosensing
Edited by Andrea Armani, Tatevik Chalyan, David Sampson

METAMATERIALS-BY-DESIGN

Theory, Technologies, and Vision

Edited by

ANDREA ALÙ
CUNY Advanced Science Research Center
CUNY Graduate Center
City University of New York (CUNY)
New York, NY, United States

NADER ENGHETA
Department of Electrical and Systems Engineering
School of Engineering and Applied Science
University of Pennsylvania
Philadelphia, PA, United States

ANDREA MASSA
ELEDIA Research Center (ELEDIA@UniTN-DICAM)
Department of Civil, Environmental, and Mechanical Engineering
Università di Trento
Trento, Italy

GIACOMO OLIVERI
ELEDIA Research Center (ELEDIA@UniTN-DICAM)
Department of Civil, Environmental, and Mechanical Engineering
Università di Trento
Trento, Italy

ELSEVIER

Elsevier
Radarweg 29, PO Box 211, 1000 AE Amsterdam, Netherlands
125 London Wall, London EC2Y 5AS, United Kingdom
50 Hampshire Street, 5th Floor, Cambridge, MA 02139, United States

Publisher's note: Elsevier takes a neutral position with respect to territorial disputes or jurisdictional claims in its published content, including in maps and institutional affiliations.

Notices

Knowledge and best practice in this field are constantly changing. As new research and experience broaden our understanding, changes in research methods, professional practices, or medical treatment may become necessary.

Practitioners and researchers must always rely on their own experience and knowledge in evaluating and using any information, methods, compounds, or experiments described herein. In using such information or methods they should be mindful of their own safety and the safety of others, including parties for whom they have a professional responsibility.

To the fullest extent of the law, neither the Publisher nor the authors, contributors, or editors, assume any liability for any injury and/or damage to persons or property as a matter of products liability, negligence or otherwise, or from any use or operation of any methods, products, instructions, or ideas contained in the material herein.

ISBN: 978-0-323-99985-4

Publisher: Matthew Deans
Acquisitions Editor: Stephen Jones
Editorial Project Manager: Palak Gupta
Production Project Manager: Fizza Fathima
Cover Designer: Greg Harris

Typeset by VTeX

Contents

Contributors

Abdelhamed Ahmed

Université Paris-Saclay, CNRS, CentraleSupélec, Laboratoire des Signaux et Systèmes, Gif-sur-Yvette, France

Andrea Alù

Photonics Initiative, Advanced Science Research Center, City University of New York, New York, NY, United States

Physics Program, Graduate Center, City University of New York, New York, NY, United States

Mirko Barbuto

"Niccolò Cusano" University, Rome, Italy

Arianna Benoni

ELEDIA Research Center (ELEDIA@UniTN - University of Trento), DICAM - Department of Civil, Environmental, and Mechanical Engineering, Trento, Italy

Filiberto Bilotti

ROMA TRE University, Rome, Italy

Jordan Budhu

Bradley Department of Electrical and Computer Engineering, Virginia Tech, Blacksburg, VA, United States

Sawyer D. Campbell

Department of Electrical Engineering and Center for Nanoscale Science, The Pennsylvania State University, University Park, PA, United States

Giuseppe Castaldi

Fields & Waves Lab, Department of Engineering, University of Sannio, Benevento, Italy

Jean Chazelas

ULTIMETAS, Paris, France

Ana Díaz-Rubio

Nanophotonics Technology Center, Universitat Politècnica de València, Valencia, Spain

Marco Di Renzo
Université Paris-Saclay, CNRS, CentraleSupélec, Laboratoire des Signaux et Systèmes, Gif-sur-Yvette, France

Nader Engheta
University of Pennsylvania, Department of Electrical and Systems Engineering, Philadelphia, PA, United States

Roberto Flamini
Huawei Technologies, Segrate (MI), Italy

Vincenzo Galdi
Fields & Waves Lab, Department of Engineering, University of Sannio, Benevento, Italy

Gabriele Gradoni
University of Surrey, Guildford, United Kingdom

Anthony Grbic
Department of Electrical Engineering and Computer Science, University of Michigan, Ann Arbor, MI, United States

Yang Hao
Queen Mary University of London, London, United Kingdom

Lei Kang
Department of Electrical Engineering and Center for Nanoscale Science, The Pennsylvania State University, University Park, PA, United States

Renato Lombardi
Huawei Technologies, Segrate (MI), Italy

YiHan Ma
Queen Mary University of London, London, United Kingdom

Stefano Maci
UNISI, Siena, Italy

Wending Mai
Department of Electrical Engineering and Center for Nanoscale Science, The Pennsylvania State University, University Park, PA, United States

Andrea Massa

ELEDIA Research Center (ELEDIA@UniTN - University of Trento), DICAM - Department of Civil, Environmental, and Mechanical Engineering, Trento, Italy

ELEDIA Research Center (ELEDIA@UESTC - UESTC), School of Electronic Engineering, Chengdu, China

ELEDIA Research Center (ELEDIA@TSINGHUA - Tsinghua University), Beijing, China

Claudio Massagrande

Huawei Technologies, Segrate (MI), Italy

Christian Mazzucco

Huawei Technologies, Segrate (MI), Italy

Massimo Moccia

Fields & Waves Lab, Department of Engineering, University of Sannio, Benevento, Italy

Alessio Monti

ROMA TRE University, Rome, Italy

Giacomo Oliveri

ELEDIA Research Center (ELEDIA@UniTN - University of Trento), DICAM - Department of Civil, Environmental, and Mechanical Engineering, Trento, Italy

Davide Ramaccia

ROMA TRE University, Rome, Italy

Marco Salucci

ELEDIA Research Center (ELEDIA@UniTN - University of Trento), DICAM - Department of Civil, Environmental, and Mechanical Engineering, Trento, Italy

Alessandro Toscano

ROMA TRE University, Rome, Italy

Sergei Tretyakov

Department of Electronics and Nanoengineering, Aalto University, Espoo, Finland

Charlotte Tripon-Canseliet

LPEM-CNRS/PSL/Sorbonne University, Paris, France

ULTIMETAS, Paris, France

Stefano Vellucci
ROMA TRE University, Rome, Italy

Francesco Verní
Huawei Technologies, Segrate (MI), Italy

Douglas H. Werner
Department of Electrical Engineering and Center for Nanoscale Science, The Pennsylvania State University, University Park, PA, United States

Eric B. Whiting
Department of Electrical Engineering and Center for Nanoscale Science, The Pennsylvania State University, University Park, PA, United States

Yuhao Wu
Department of Electrical Engineering and Center for Nanoscale Science, The Pennsylvania State University, University Park, PA, United States

Jingwei Xu
Department of Electrical Engineering and Center for Nanoscale Science, The Pennsylvania State University, University Park, PA, United States

Alessio Zappone
University of Cassino and Lazio Meridionale, Cassino, Italy

CHAPTER 1

Metamaterials-by-Design: introduction and paradigm

Andrea Alù[a,b], **Nader Engheta**[c], **Andrea Massa**[d,e,f], **and Giacomo Oliveri**[d]

[a]Photonics Initiative, Advanced Science Research Center, City University of New York, New York, NY, United States
[b]Physics Program, Graduate Center, City University of New York, New York, NY, United States
[c]University of Pennsylvania, Department of Electrical and Systems Engineering, Philadelphia, PA, United States
[d]ELEDIA Research Center (ELEDIA@UniTN - University of Trento), DICAM - Department of Civil, Environmental, and Mechanical Engineering, Trento, Italy
[e]ELEDIA Research Center (ELEDIA@UESTC - UESTC), School of Electronic Engineering, Chengdu, China
[f]ELEDIA Research Center (ELEDIA@TSINGHUA - Tsinghua University), Beijing, China

1.1 Introduction

In recent years, the concept of engineering artificial materials with specific effective physical properties has become a fundamental aspect in various advanced fields, such as microwave technology, terahertz systems, photonics, and optics. The ability to achieve desired performance, features, and flexibility by combining common materials through suitable mixtures or ordered arrangements has captivated a diverse community of interdisciplinary experts, including electrical and mechanical engineers, physicists, chemists, material scientists, computer scientists, and mathematicians, to name a few. This has given rise to the exciting domain of metamaterial science and engineering, with a wide variety of significant applications already showcased in both academic and industrial settings. Within this framework, the community has recently witnessed a gradual but steady shift regarding the methodological and technological approaches to metamaterial synthesis. Whereas early strategies relied heavily on techniques and material architectures allowing to obtain a certain material equivalent property (i.e., refractive index, permittivity, permeability, etc.), current approaches more often aim at synthesizing artificial materials delivering an "overall" performance in terms of system-level figures of merit or quality factors.

This growing trend naturally presents a multitude of new opportunities for both research and industrial pursuits. Designers can indeed focus

Metamaterials-by-Design
https://doi.org/10.1016/B978-0-32-399985-4.00007-6

their attention on actual measurable system objectives since the beginning of the design process, disregarding micro-scale properties and equivalence issues. However, this shift towards innovative system-performance-driven metamaterial design methods brings with it considerable challenges from the standpoint of modeling and synthesis. Unlike more traditional approaches based on "periodic" or "quasi-periodic" simplified formulations, these methods require the incorporation of multi-scale, and possibly multi-physics, modeling of artificial materials, alongside advanced optimization and synthesis techniques. The central motivation for this volume is therefore to discuss the current advancements in theory, techniques, and the exciting prospects in this field. More specifically, this volume is devoted to a comprehensive review of the latest advancements and current trends in the field of system-level-oriented metamaterial design methods, technologies, and future perspectives. Starting from the theoretical and methodological motivations to macro-scale performance-driven design of volumetric and planar metamaterials, the volume introduces and details advanced task-oriented modeling approaches with specific reference to their multi-scale / multi-physics customization in recent metamaterial science and engineering. Afterwards, a broad set of recent application examples in microwave, terahertz, photonics, and optics scenarios are discussed in a parallel fashion, but highlighting the rational and methodological interconnections among the different domains, including active and passive metamaterial-enhanced devices for communications and sensing, with contributions from both the industry and the academia.

The concluding chapters of this volume aim at offering a visionary outlook on the present trends and forthcoming research and practical directions in system-performance-driven metamaterial design methodologies and technologies. This includes exploring potential applications in future reconfigurable and deep-learning driven metamaterials. By examining these aspects, we hope to shed light on the promising possibilities that lie ahead and inspire further exploration and innovation in the field of metamaterial science and engineering.

This volume is tailored for a diverse audience, including PhD students, researchers, scientists, applied mathematicians, and engineers in the fields of electrical engineering, telecommunications, microwaves, optics, and plasmonics. It caters to individuals both from academia and industry who have an interest in the following aspects:

(a) Learning the fundamentals of metamaterial-by-design (MbD).

(b) Enhancing the knowledge of MbD modeling, design, and technological approaches.
(c) Understanding the latest advancements in MbD applications, particularly in the domains of wireless communications and sensing.
(d) Gaining an overview of both academic and industrial perspectives on task-oriented materials.

By addressing these topics, the volume aims at providing a comprehensive and valuable resource for all those looking to delve into the fascinating world of metamaterial-by-design and its practical applications across various domains.

1.2 Overview of the volume

The first part of the Volume is dedicated to providing a comprehensive review of the concepts, ideas, and methodologies in metamaterial-by-design. This section explores a wide spectrum of innovative approaches, theoretical foundations, and practical strategies that play a pivotal role in shaping the dynamic landscape of metamaterial synthesis. Moreover, it offers an exploration of cutting-edge advancements and breakthroughs, showcasing the latest developments in the realm of metamaterial-by-design strategies with an emphasis on fostering a strong theoretical and conceptual frameworks.

In [1], Tretyakov and Díaz-Rubio present an analytical framework on modeling and designing reflective metasurfaces, aiming to facilitate the practical implementation of meta-atoms composing the metasurface. In particular, reflective metasurfaces are treated as impenetrable boundaries, where fields behind the metasurface are zero, and the electromagnetic response is determined by the relation between the electric and magnetic fields in the illumination half-space. These metasurfaces can be engineered for various functionalities, including field concentration for sensing enhancement, absorption, polarization conversion, or control of the reflection direction. Among such examples, the ability to control the direction of wave reflection has been extensively studied due to its relevance in multiple scenarios across different frequency ranges, such as smart communication systems and light detection and ranging. A common example is the so-called "anomalous reflection," and although seemingly simple, it possesses intricate and disguised properties. The authors detail the modeling and design processes of such classes of bidimensional metamaterials, providing valuable insights for their integration into real-world environments.

impedance

$$Z_{\text{inp}} = jZ_{\text{d}} \tan(k_{\text{d}}\ell), \tag{2.29}$$

with Z_{d} and k_{d} being the electromagnetic wave impedance and the wavenumber in the medium that fills the grove, respectively.

2.2 Multi-physics methodology

2.2.1 Control of acoustic waves

The design approach presented in the previous section is not only applicable to electromagnetic waves. In this section, we will describe the formalism for designing acoustic power flow-conformal metamirrors. Here we will focus on engineering a set of two acoustic waves: an incident wave and a reflected wave. We will start defining the pressure field generated by two plane waves. Following the same notations as in the electromagnetic scenario, we assume xz-plane to be the plane of incidence, while θ_{i} and θ_{r} define the propagation directions of the incident and reflected plane waves, respectively. In these notations, the pressure field reads

$$p(x, z) = p_{\text{i}} e^{-j\mathbf{k}_{\text{i}}\cdot\mathbf{r}} + p_{\text{r}} e^{-j\mathbf{k}_{\text{r}}\cdot\mathbf{r}}, \tag{2.30}$$

where the wavenumbers $\mathbf{k}_{\text{i}} = k(\sin\theta_{\text{i}}\hat{\mathbf{x}} - \cos\theta_{\text{i}}\hat{\mathbf{z}})$ and $\mathbf{k}_{\text{r}} = k(\sin\theta_{\text{r}}\hat{\mathbf{x}} + \cos\theta_{\text{r}}\hat{\mathbf{z}})$ have the same definition as in the electromagnetic scenario, and $p_{\text{i}} = |p_{\text{i}}|e^{j\phi_{\text{i}}}$ and $p_{\text{r}} = |p_{\text{r}}|e^{j\phi_{\text{r}}}$ represent the complex amplitudes of the incident and reflected waves. By recognizing that $\vec{v} = j\nabla p/\omega\rho$, the velocity field can be written as

$$v_x(x, z) = \frac{k}{\omega\rho}\left[p_{\text{i}} \sin\theta_{\text{i}} e^{-j\mathbf{k}_{\text{i}}\cdot\mathbf{r}} + p_{\text{r}} \sin\theta_{\text{r}} e^{-j\mathbf{k}_{\text{r}}\cdot\mathbf{r}}\right], \tag{2.31}$$

$$v_y(x, z) = \frac{k}{\omega\rho}\left[-p_{\text{i}} \cos\theta_{\text{i}} e^{-j\mathbf{k}_{\text{i}}\cdot\mathbf{r}} + p_{\text{r}} \cos\theta_{\text{r}} e^{-j\mathbf{k}_{\text{r}}\cdot\mathbf{r}}\right], \tag{2.32}$$

where ω is the angular frequency, and ρ is the density of the background media. Using this definition of the acoustic fields, the intensity vector of the superposition of both incident and reflected plane waves can be calculated as $\boldsymbol{I}(x, z) = \frac{1}{2}\Re(p\boldsymbol{v}^*) = I_x(x, z)\hat{\mathbf{x}} + I_z(x, z)\hat{\mathbf{z}}$. The analytical expression for

the flow of power carried by two arbitrary acoustic plane waves reads

$$\begin{aligned} I_x(x,z) =& \frac{k}{2\omega\rho}\left[|p_\mathrm{i}|^2\sin\theta_\mathrm{i} + |p_\mathrm{r}|^2\sin\theta_\mathrm{r}\right] \\ &+ \frac{k}{2\omega\rho}|p_\mathrm{i}||p_\mathrm{r}|(\sin\theta_\mathrm{i} + \sin\theta_\mathrm{r})\cos(\Delta\mathbf{k}\cdot\mathbf{r} + \Delta\phi), \end{aligned} \tag{2.33}$$

and

$$\begin{aligned} I_z(x,z) =& \frac{k}{2\omega\rho}\left[-|p_\mathrm{i}|^2\cos\theta_\mathrm{i} + |p_\mathrm{r}|^2\cos\theta_\mathrm{r}\right] \\ &+ \frac{k}{2\omega\rho}\left[|p_\mathrm{i}||p_\mathrm{r}|(\cos\theta_\mathrm{r} - \cos\theta_\mathrm{i})\cos(\Delta\mathbf{k}\cdot\mathbf{r} + \Delta\phi)\right], \end{aligned} \tag{2.34}$$

where $\Delta\mathbf{k} = \mathbf{k}_\mathrm{r} - \mathbf{k}_\mathrm{i}$ and $\Delta\phi = \phi_\mathrm{i} - \phi_\mathrm{r}$.

As it was demonstrated for the electromagnetic counterpart, for ensuring perfect conversion between the incident and reflected plane waves and avoiding scattering of energy into any other direction, the amplitude of the reflected wave has to satisfy $|p_\mathrm{r}| = |p_\mathrm{i}|\sqrt{\cos\theta_\mathrm{i}/\cos\theta_\mathrm{r}}$. Using this relation and knowing that the acoustic wave impedance is defined as $\eta_0^\mathrm{ac} = \omega\rho/k$, the x and z components of the intensity vector can be simplified as

$$I_x(x,z) = I_0\left[\sin\theta_\mathrm{i} + |R|^2\sin\theta_\mathrm{r} + |R|(\sin\theta_\mathrm{i} + \sin\theta_\mathrm{r})\cos(\Delta\mathbf{k}\cdot\mathbf{r} + \Delta\phi)\right], \tag{2.35}$$

and

$$I_z(x,z) = I_0\left[|R|(\cos\theta_\mathrm{r} - \cos\theta_\mathrm{i})\cos(\Delta\mathbf{k}\cdot\mathbf{r} + \Delta\phi)\right], \tag{2.36}$$

where $I_0 = \frac{1}{2}\frac{|p_\mathrm{i}|^2}{\eta_0^\mathrm{ac}}$ and $|R| = \frac{|p_\mathrm{r}|}{|p_\mathrm{i}|} = \sqrt{\cos\theta_\mathrm{i}/\cos\theta_\mathrm{r}}$.

Following the design methodology of power-flow metamirrors, we define a vector perpendicular to the intensity vector as $\mathbf{N} = -I_y\hat{\mathbf{x}} + I_x\hat{\mathbf{y}}$. Then we define a scalar function $g(x,y)$ such that $\nabla g(x,y) = \mathbf{N}$. The analytical expression for the function $g(x,z)$ reads

$$g(x,z) = I_0\left[Ay + B\sin\left(\Delta\mathbf{k}\cdot\mathbf{r}\right) + C\right], \tag{2.37}$$

where $A = \sin\theta_\mathrm{i} + |R|^2\sin\theta_\mathrm{r}$, $B = \frac{|R|}{k}\frac{\cos\theta_\mathrm{i} - \cos\theta_\mathrm{r}}{\sin\theta_\mathrm{i} - \sin\theta_\mathrm{r}}$, and C is a constant. Notice that this expression is similar to the one derived for the electromagnetic counterpart [see Eq. (2.12)]. There is a clear analogy between the two physical problems: For TM-polarized waves, the amplitude of magnetic fields

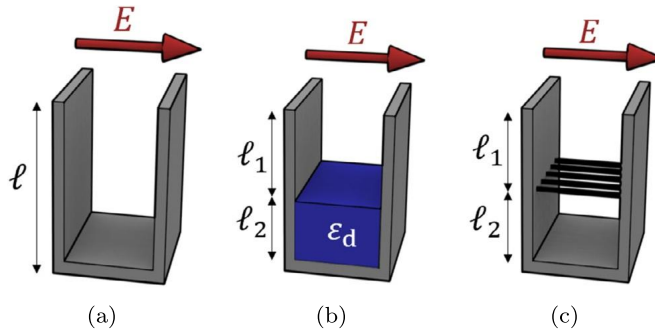

Figure 2.9 ***Dual-physics meta-atoms.*** (a) Empty closed-end groves. (b) Partially filled closed-end groves. (c) Closed-end groves with a metallic grid.

plays the role of the amplitude of the pressure fields ($p_{\mathrm{i,r}} \rightarrow H_{\mathrm{i,r}}$), and the density of the background media is analogous to the permittivity ($\rho \rightarrow \varepsilon_0$). For TE-polarized waves, the amplitude of the pressure fields is analogous to the amplitude of electric fields ($p_{\mathrm{i,r}} \rightarrow E_{\mathrm{i,r}}$), and the density of the background media is analogous to the permeability ($\rho \rightarrow \mu_0$). This analogy can be used for designing dual-physics metamirrors capable to manipulate waves of different nature in a single device.

2.2.2 Dual-physics metamirrors

In this section, we will show that by exploiting the concept of power flow-conformal metamirrors and the analogy between the electromagnetic and acoustic scenarios, it is possible to create metasurfaces that operate simultaneously for both acoustic and electromagnetic waves. We can distinguish two different types of dual-physics metamirrors: (i) same functionality for electromagnetic and acoustic waves and (ii) different functionalities for acoustic and electromagnetic waves. To design such devices, we need to ensure that the surface profiles required for both operations are compatible and proper implementation of the corresponding surface impedance for both acoustic and electromagnetic functionalities to be feasible.

The main challenge in both cases is to find meta-atoms that will provide desired surface impedance both for acoustic and electromagnetic waves. Here we describe three different structures that can be used to achieve this goal. Fig. 2.9 shows the proposed meta-atoms. As we will see later, the choice between them will be made based on specific conditions in each design.

inversion. The analog to (4.31) for the transmissive metasurface of Fig. 4.5a is [6]:

$$\begin{bmatrix} [V_1] \\ [V_2] \\ [V_3] \\ [V_4] \\ [V_5] \end{bmatrix} = \left(\begin{bmatrix} [Z_{s1}] & 0 & 0 & 0 & 0 \\ 0 & [Z_{s2}] & 0 & 0 & 0 \\ 0 & 0 & [Z_{s3}] & 0 & 0 \\ 0 & 0 & 0 & [Z_{s4}] & 0 \\ 0 & 0 & 0 & 0 & [Z_{s5}] \end{bmatrix} + \begin{bmatrix} [Z_{11}] & [Z_{12}] & [Z_{13}] & [Z_{14}] & [Z_{15}] \\ [Z_{21}] & [Z_{22}] & [Z_{23}] & [Z_{24}] & [Z_{25}] \\ [Z_{31}] & [Z_{32}] & [Z_{33}] & [Z_{34}] & [Z_{35}] \\ [Z_{41}] & [Z_{42}] & [Z_{43}] & [Z_{44}] & [Z_{45}] \\ [Z_{51}] & [Z_{52}] & [Z_{53}] & [Z_{54}] & [Z_{55}] \end{bmatrix} \right) \begin{bmatrix} [I_1] \\ [I_2] \\ [I_3] \\ [I_4] \\ [I_5] \end{bmatrix}, \quad (4.33)$$

which can also be written in the form of (4.32).

4.4.2 Numerical design algorithm

An aperiodic metasurface modeled with integral equations is designed in three phases, as depicted in Fig. 4.7. In Phase 1, the desired total field is stipulated and the integral equations (4.32) are solved to obtain the unknown currents. Then (4.28) is used to determine the sheet impedances. Since an arbitrarily defined field transformation may not lead to conserved normal local power density across the plane of the metasurface, the resultant sheet impedances may be complex-valued, necessitating lossy or active (amplifying) sheet elements [7], [25], [26]. In Phase 2, the lossy or active sheet impedance elements are removed by performing gradient descent optimization on the impedance sheets obtained from Phase 1. Finally, in Phase 3, the purely reactive sheets are realized as patterned metallic claddings. The following sections detail each phase. The previous design examples will then be redesigned using the three-phase numerical approach.

4.4.2.1 Phase 1: Direct solve of integral equations

Phase 1 of metasurface design using the integral equation modeling approach can be summarized in the following steps:

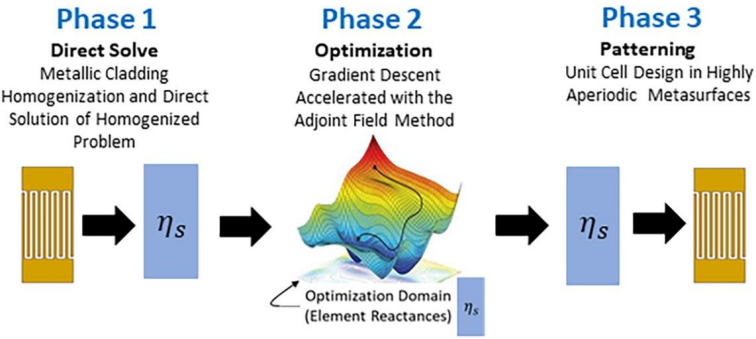

Figure 4.7 Three phase metasurface design cycle.

1. In the case of transmissive metasurfaces, define the desired total field on the input side (layer 1) and the output side (layer 5) of the metasurface. In the case of reflection, define the desired total field only on the input side (layer 1). The total field will be the phasor summation of the incident field plus a stipulated scattered field. Ensure global aperture field power is conserved when defining the total fields (see (4.36) and (4.38)).
2. Eliminate an unknown sheet impedance in the linear systems by making the substitution $E_1^{tot} = Z_{s1}J_{s1}$ on the input side (layer 1) and $E_5^{tot} = Z_{s5}J_{s5}$ on the output side (layer 5). For the middle sheet impedance, use Z_{s2} from (4.20) since the total field cannot be explicitly defined along this layer. For the reflection case, only make the substitution for the input side $E_1^{tot} = Z_{s1}J_{s1}$. The system of equations in both transmissive and reflective cases are now linear and can be solved.
3. Solve the linear system (4.32).
4. Obtain the sheet impedances by applying (4.28) for each unknown sheet impedance layer.

The design algorithm will be applied to the design examples next.

Design Example 1*: Transmissive metasurface that collimates and refracts a line source*

In step 1 of Phase 1, the desired total field on the input side is simply the incident field given by (4.24), since the metasurface should be reflectionless. Defining $[W_1] = [Z_{s1}][I_1] = [V_1]$, where $[V_1]$ is formed by testing (4.24)

with the same expansion functions used to expand the currents (Galerkin's Method), (4.33) becomes

$$\begin{bmatrix} [V_1]-[W_1] \\ [V_2] \\ [V_3] \\ [V_4] \\ [V_5] \end{bmatrix} = \left(\begin{bmatrix} 0 & 0 & 0 & 0 & 0 \\ 0 & [Z_{s2}] & 0 & 0 & 0 \\ 0 & 0 & [Z_{s3}] & 0 & 0 \\ 0 & 0 & 0 & [Z_{s4}] & 0 \\ 0 & 0 & 0 & 0 & [Z_{s5}] \end{bmatrix} + \begin{bmatrix} [Z_{11}] & [Z_{12}] & [Z_{13}] & [Z_{14}] & [Z_{15}] \\ [Z_{21}] & [Z_{22}] & [Z_{23}] & [Z_{24}] & [Z_{25}] \\ [Z_{31}] & [Z_{32}] & [Z_{33}] & [Z_{34}] & [Z_{35}] \\ [Z_{41}] & [Z_{42}] & [Z_{43}] & [Z_{44}] & [Z_{45}] \\ [Z_{51}] & [Z_{52}] & [Z_{53}] & [Z_{54}] & [Z_{55}] \end{bmatrix} \right) \begin{bmatrix} [I_1] \\ [I_2] \\ [I_3] \\ [I_4] \\ [I_5] \end{bmatrix}. \tag{4.34}$$

The desired total field on the output side can be found by locally conserving normal power across the plane of the metasurface. Hence the desired output total field is set to

$$E_5^{tot} = E_5^{sca} = \sqrt{\frac{2\eta_0 S_y^{inc}}{\cos\theta_t}} e^{jk_0(x\sin\theta_t - 2d\cos\theta_t)}, \tag{4.35}$$

where S_y^{inc} is the normal power density of the incident field (see the appendix of [7]), and θ_t is the transmitted plane wave field angle. Note that (4.35) conserves global power, since

$$\int_{-w/2}^{w/2} \frac{1}{2}\left[\vec{E}_5^{sca} \times \vec{H}_5^{sca^*}\right] dx = \int_{-w/2}^{w/2} \frac{1}{2}\left[\vec{E}_1^{inc} \times \vec{H}_1^{inc^*}\right] dx = P^{inc}. \tag{4.36}$$

The substitution $[W_5] = [Z_{s5}][I_5]$ can be made in the linear system by again testing the (4.35) with the same expansion functions used to represent the current. The impedances Z_{s2} and Z_{s4} are defined from volume equivalence, and Z_{s3} is defined using the second equation of (4.20). The linear system can now be solved through matrix inversion. Thus in design step 3, (4.32) is solved for the induced currents, and in design step 4, the sheets are found following (4.28). This results in the impedance sheets shown in Fig. 4.8a. The middle sheet is the same as in Fig. 4.5b by construction. Both the upper and lower sheets, Z_{s1} and Z_{s5}, are complex-valued, since local power density is not conserved at those sheets. That is, the normal power entering layer 1 is equal to the normal power exiting layer 5, but not equal to that exiting layer 1. In Fig. 4.8b and 4.8c, the electric near

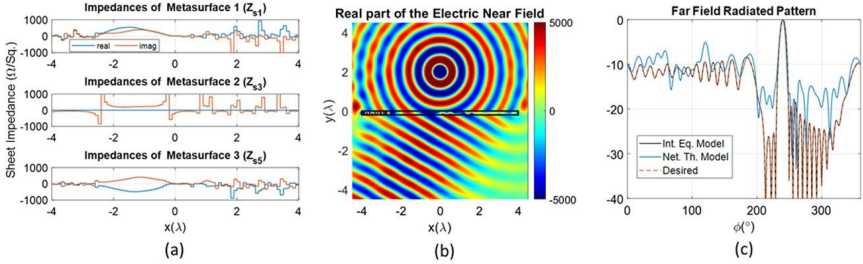

Figure 4.8 Metasurface design example 1, Numerical design, Phase 1. (a) Complex-valued sheet impedance for the impedance sheet layers. (b) Near electric field. (c) Far electric field.

and far fields are shown. The near field shows much better adherence to the design stipulations than those in Fig. 4.5a. This is due to the more accurate modeling of the integral equation technique, which models the true thickness of the metasurface and all mutual coupling between cells, both the intra- and inter-layer. The improved modeling is evident in the far field plot. The back lobe region ($0 \leq \phi \leq 180°$) shows some edge diffraction from both finite metasurface edges but otherwise no reflections, indicating a matched metasurface. In the forward region, the beam is formed in the correct direction with deep nulls and low sidelobes.

***Design Example 2**: Reflective metasurface that collimates and reflects a line source*
In step 1 of Phase 1, the total field on the impedance sheet is defined as the incident field plus the desired scattered field:

$$E_1^{tot} = E_1^{inc} + E_1^{sca} = -\frac{I_0 \eta_0 k_0}{4} H_0^{(2)}\left(k_0\sqrt{x^2+F^2}\right) + \sqrt{\frac{2\eta_0 S_y^{inc}}{\cos\theta_t}} e^{jk_0 x \sin\theta_t}. \quad (4.37)$$

Note that (4.37) also conserves global power since

$$\int_{-w/2}^{w/2} \frac{1}{2}\left[\vec{E}_1^{\,sca} \times \vec{H}_1^{\,sca^*}\right] dx = \int_{-w/2}^{w/2} \frac{1}{2}\left[\vec{E}_1^{\,inc} \times \vec{H}_1^{\,inc^*}\right] dx = P^{inc}. \quad (4.38)$$

In step 2, the substitution of $[W_1] = [Z_{s1}][I_1]$ into (4.31) can be made by again testing (4.37) with the same expansion functions used to represent the currents. Then, in step 3, the linear system is solved for the induced currents. Finally, in step 4, the sheet impedance is backed out using (4.28). The resulting impedance sheet is shown in Fig. 4.9a. The sheet impedances are complex-valued, since local power density is again

which yields $\max_{\theta,\phi} D(\theta,\phi) = 2$, and hence

$$\gamma_{abs} \approx \frac{1}{2\pi}\left(\frac{\lambda}{Nd}\right)^2. \tag{6.11}$$

By observing such scaling law in Fig. 6.2 (magenta-dashed-dotted line), we note a considerable margin (∼12 dB) for further reduction of the RCS ratio with respect to the optimized-coding results. However, the condition in Eq. (6.10) requires a spectral shaping that is rather unrealistic, and therefore we expect the absolute lower bound in Eq. (6.11) to be quite *loose*.

For a tighter bound, we assume an *isotropic array factor* (IAF), $|\Lambda(\kappa)| =$ constant, which is a more realistic condition. By substituting this assumption in Eq. (6.4), we obtain a metasurface directivity coinciding with the supercell directivity. Assuming, as a realistic setting, a supercell of sidelength $d = \lambda$ comprising 7×7 unit cells, this yields the scaling law

$$\gamma_{IAF} \approx \frac{15.01}{4\pi}\left(\frac{\lambda}{Nd}\right)^2, \tag{6.12}$$

also shown (purple-dashed line) in Fig. 6.2. Quite interestingly, the above IAF bound turns out to be close to (∼3 dB below) the optimized-coding results. This indicates that a possible sub-optimal design strategy could be aimed at "flattening" the array-factor response.

6.2.4 Suboptimal spatial coding

The IAF condition is inherently tied with a celebrated problem in pure mathematics concerning the so-called "flat polynomials." Loosely speaking, this problem concerns to what extent the absolute value of a polynomial with quantized coefficients can be made *almost constant* on the unit circle. Although such problem remains elusive and largely open, there are several theoretical results and conjectures available [17–21] (see also the discussion in [15]). Interestingly, it has been shown that a completely random choice of the coefficients is far from optimal [19]. A viable option, in terms of tradeoff between "flatness" and computational burden, is provided by the Golay—Rudin–Shapiro (GRS) polynomials [22–24], which can be defined recursively as

$$\begin{aligned} P_{\nu+1}(\xi) &= P_\nu(\xi) + \xi^{2^\nu} Q_\nu(\xi), \\ Q_{\nu+1}(\xi) &= P_\nu(\xi) - \xi^{2^\nu} Q_\nu(\xi), \end{aligned} \tag{6.13}$$

with $P_0 = Q_0 = 1$. This leads to a rather straightforward and computationally inexpensive synthesis of a coded metasurface, irrespective of the

electrical size of the target. Basically, for a chosen sequence length and type (P or Q), the local reflection coefficients $\Gamma_n \in \{-1, 1\}$ can be directly calculated as polynomial coefficients from the recursive definitions in Eqs. (6.13), via symbolic-manipulation tools. Alternatively, the coefficients can be explicitly obtained by means of an auxiliary binary sequence with the alphabet $\{-1, 1\}$,

$$\varsigma_0 = 1, \quad \varsigma_{2n} = \varsigma_n, \quad \varsigma_{2n+1} = (-1)^n \varsigma_n, \tag{6.14}$$

which, for $N = 2^\nu$, directly yields the reflection-coefficient sequence pertaining to the P_ν-type polynomials,

$$\Gamma_n = \varsigma_n, \quad n = 0, ..., N-1, \tag{6.15}$$

and, with a sign flip in the second half, also yields the sequence pertaining to the Q_ν-type polynomials

$$\Gamma_n = \begin{cases} \varsigma_n, & n = 0, ..., \frac{N}{2} - 1, \\ -\varsigma_n, & n = \frac{N}{2}, ..., N-1. \end{cases} \tag{6.16}$$

For the same unit-cell, supercell, and operational frequency as for the optimized-coding results in Fig. 6.2. Fig. 6.3 shows the numerically (full-wave) computed 3-D RCS patterns for representative GRS designs, featuring P_ν- and Q_ν-type coding, with $\nu = 3$ (8×8 supercells, i.e., $8\lambda \times 8\lambda$ total size) and $\nu = 4$ (16×16 supercells, i.e., $16\lambda \times 16\lambda$ total size). The sought diffuse-scattering response is observed, with reasonably uniform distributions of peaks. Fig. 6.4 shows the corresponding RCS-ratio scaling laws, with the full-wave (finite-element) results limited to orders $\nu = 3$ and $\nu = 4$ (cf. Fig. 6.3; compatible with our current computational resources), and the semi-analytical results shown for orders up to $\nu = 7$ (corresponding to a maximum total size of $128\lambda \times 128\lambda$). The very good agreement with the full-wave predictions validates the semi-analytical modeling, which can be utilized also for electrically large structures. Once again, we observe fairly linear trends for the scaling laws, with slopes very similar to the IAF bound, and only few dB differences in the intercepts, attributable to the imperfect flatness of the GRS polynomials. The algebraic numerical fits yield

$$\gamma_{GRSP} \approx 4.375 \left(\frac{\lambda}{Nd}\right)^{1.991}, \quad \gamma_{GRSQ} \approx 2.73 \left(\frac{\lambda}{Nd}\right)^{1.902}, \tag{6.17}$$

which are quantitatively consistent with the optimized-coding ones in Eq. (6.7). However, unlike brute-force optimization, our proposed GRS-

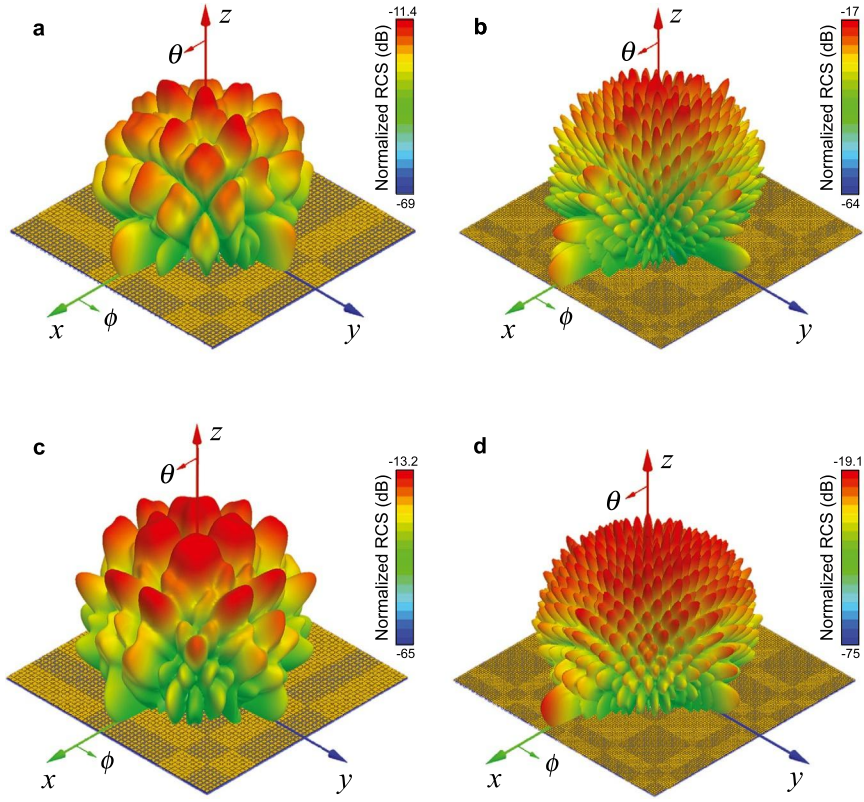

Figure 6.3 (a), (b) Numerically computed 3-D RCS patterns pertaining to P_3 and P_4 GRS coding, respectively, superposed on the corresponding metasurface patterns (not in scale), with parameters as in Fig. 6.2. Results are normalized with respect to the maximum RCS of a PEC target of same size. (c), (d) Same as above, but for Q_3 and Q_4 coding, respectively. Credit: M. Moccia, S. Liu, R.Y. Wu, G. Castaldi, A. Andreone, T.J. Cui, V. Galdi, Coding metasurfaces for diffuse scattering: Scaling laws, bounds, and suboptimal design, Advanced Optical Materials. 5 (2017) 1700455–11. https://doi.org/10.1002/adom.201700455.

coding design can be inexpensively applied to metasurfaces with *arbitrarily large* sizes.

6.2.5 Space-time coding

In programmable digital coding metasurfaces, dynamic modulation of the local reflection coefficients provides additional degrees of freedom, granting

priate boundary conditions are applied at each TB. Hence we classify these problems as "Temporal Boundary Value Problems (TBVPs)."

7.3.3 Temporal boundary value problems: simple systems

First, we provide a review of TBVPs in relatively simple material systems, which share some common characteristics: isotropic, non-dispersive, lossless, and homogeneous.

a. ***Effective medium***

Pacheco-Peña et al., introduced some pioneering concepts on the time domain counterpart of effective medium theory. For instance, they investigated the concept of a temporal effective medium. [58] It was found that a temporal multi-layer structure, whose permittivity alternates between two values in time, can be equivalently modeled by an effective medium followed by a step function in time. Moreover, it was shown that the effective medium could be expressed as a function of the permittivities and duty cycle of the alternating temporal layers, after some mathematical manipulations. Therefore one can easily engineer the properties of an effective medium in the time domain, as is done historically in the spatial case.

b. ***Anti-reflection temporal coating (ATC)***

In [58], the authors developed the concept of an "anti-reflection temporal coating (ATC)." As we know from Section 7.2, a TB would cause reflection, and therefore it is important to develop a temporal method in order to minimize reflection. To this end, by temporally inserting an intermediate layer whose permittivity and duration are engineered, the resulting reflection can be effectively reduced. The duration of the intermediate temporal layer should be $(2\mathrm{N}+1)/4T_0$, where $\mathrm{N} = 1, 2, 3\ldots$, and T_0 is the period of the wave. This result is reminiscent of the traditional quarter-wave transformer, where the intermediate layer has a length of $1/4^{\text{th}}$ of a wavelength. The authors employ this technique to match the impedance of two waveguides with mismatched cross-sectional areas. The schematics and simulated results of an ATC are shown in Figs. 7.5(a) and 7.5(b).

Later, the notion of an ATC is further exploited in other works. In [58], the authors noticed that when the duration of the intermediate temporal layer is increased to $1/2T_0$, the device would be analogous to a Fabry-Perot cavity. Coincidently, the so called "time-domain Fabry-Perot resonator" was developed and investigated in the case where materials are dispersive, where the authors also developed a scheme to equivalently create TBs using

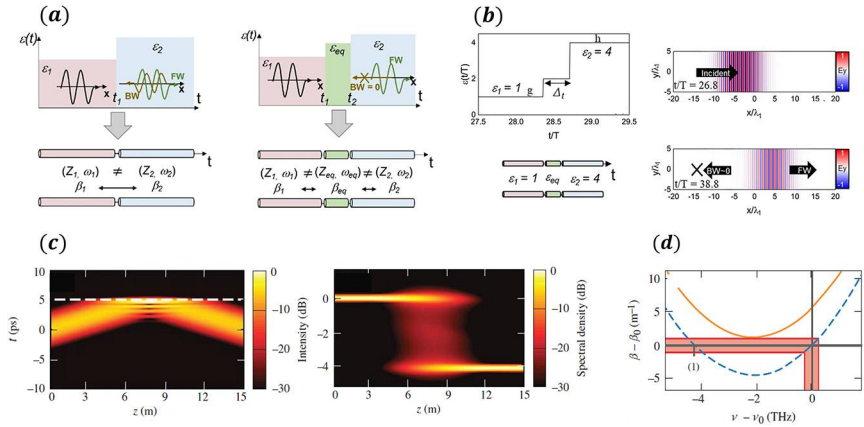

Figure 7.5 (a) Schematic representation of a single temporal boundary (left), and a temporal analogue of a quarter-wave transformer (right). The equivalent transmission-line model is shown in the bottom figure of each panel. (b) Temporal function of permittivity along with the equivalent transmission-line model for a temporal quarter-wave transformer (left), and numerical results of the electric field distribution at different times showing the incident and transmitted waves of a narrowband pulse without reflection when using the temporal impedance-matching technique (right). (c) Evolution of pulse shape (left), and spectrum (right) in the presence of a temporal boundary (dashed white line) for $\beta_B = 5.6\, m^{-1}$. (d) Dispersion curves for $t < T_B$ (dashed blue) and $t > T_B$ (solid orange). The red-shaded region shows the spectral extent of the input pulse and the corresponding range of propagation constants. ((a)(b) are reprinted from ref[100], and (c)(d) are reprinted from ref[86]).

a pump-probe configuration. Mai et al. studied the transmission behavior in ATCs, and found that the energy of such a temporal system is not preserved. [62] In [85], Pacheco-Peña et al. generalize the ATC to an impedance transformer by using multiple, rather than just one, intermediate layers. With more degrees of freedom, it was shown that the spectral response of temporal devices can be engineered to better tailor the properties of electromagnetic waves.

c. *Temporal waveguides*

Waveguides represent an important device that can constrain and control the propagation of electromagnetic waves, so that the transmission of energy can be effectively guided from one location to another. Their oper-

CHAPTER 9

Digital reconfigurable intelligent surfaces: on the impact of realistic reradiation models

Analysis of sub-wavelength implementations, quantization of the reflection coefficient, interplay between the amplitude and phase of the reflection coefficient, near-field and far-field regions, electromagnetic interference

Marco Di Renzo[a], **Abdelhamed Ahmed**[a], **Alessio Zappone**[b], **Vincenzo Galdi**[c], **Gabriele Gradoni**[d], **Massimo Moccia**[c], **and Giuseppe Castaldi**[c]

[a]Université Paris-Saclay, CNRS, CentraleSupélec, Laboratoire des Signaux et Systèmes, Gif-sur-Yvette, France
[b]University of Cassino and Lazio Meridionale, Cassino, Italy
[c]Fields & Waves Lab, Department of Engineering, University of Sannio, Benevento, Italy
[d]University of Surrey, Guildford, United Kingdom

9.1 Introduction

9.1.1 Reconfigurable intelligent surfaces and holographic surfaces

In the last few years, intelligent surfaces have been the subject of extensive research activities in the context of wireless communications and networks [1], [2], [3], [4], [5]. A recent roadmap can be found in [6]. In essence, an intelligent surface is a dynamic metasurface, which shapes the reradiated electromagnetic waves as desired, thanks to a careful design of elementary scattering elements and to an appropriate optimization of simple electronic circuits [7]. In wireless communications, intelligent surfaces have been researched for several applications, and mainly for two possible uses:

1. **Nearly-passive reconfigurable devices** that are capable of shaping the electromagnetic waves that impinge upon them [8]. Two typical examples are surfaces that reflect or refract, e.g., smart windows, the

Metamaterials-by-Design
https://doi.org/10.1016/B978-0-32-399985-4.00017-9

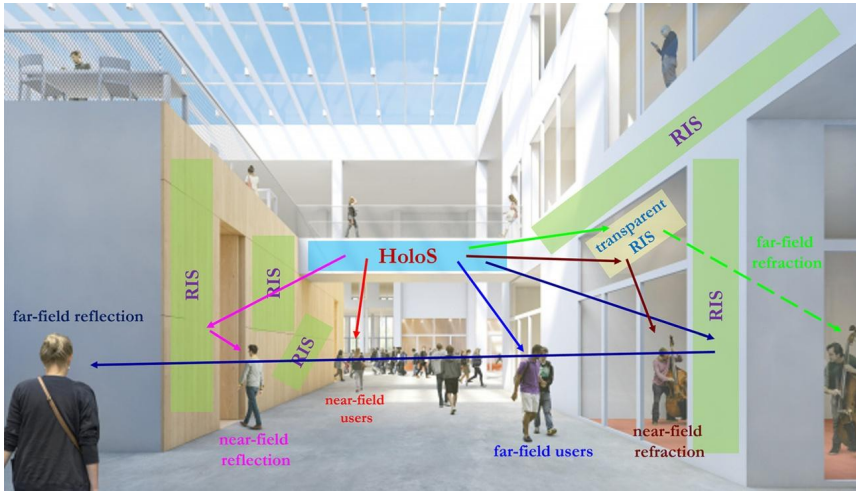

Figure 9.1 Emerging wireless communication scenario with far-field and near-field users.

electromagnetic waves towards non-specular directions. These surfaces are usually referred to as reconfigurable intelligent surfaces (RISs) [9].

2. **Low-complexity active transceivers** that are capable of realizing extremely massive multiple-input multiple-output communications [10]. These surfaces are usually referred to as dynamic metasurface antennas (DMAs) [11] or holographic surfaces (HoloSs) [12].

The main advantage of an RIS consists of controlling the propagation environment besides the end points of a transmission link, i.e., transmitters and receivers, without the need of requiring power amplifiers, radio frequency chains, and digital signal processors. An RIS operates in the wave domain directly on the electromagnetic waves. The main advantage of a HoloS consists of being equipped with a very large number of reconfigurable metamaterial elements (like an RIS) but with a limited number of radio frequency chains. This feature is highly desirable, since it reduces the number of radio frequency chains, while offering higher beamforming and spatial multiplexing gains [11]. Notably, these surfaces, if sufficiently large in size, may provide spatial multiplexing gains, i.e., multiple orthogonal communication modes, even in free-space line-of-sight propagation environments [13], [14], [15]. In wireless communication systems and networks, RISs and HoloSs are jointly deployed in the environment to boost the communication performance. An illustration of this emerging communication scenario is shown in Fig. 9.1.

Specifically, thanks to their expected large electrical size, RISs and HoloSs may bring fundamentally new challenges to the design and optimization of wireless networks. One of them is the need of engineering and optimizing wireless communication networks whose devices may likely operate in the near-field of each other, and therefore the electromagnetic waves can no longer be assumed to be characterized by a planar wavefront, but a spherical wavefront needs to be accounted for at the design stage [16]. Also the possibility of packing on an intelligent surface hundreds or thousands of radiating elements at sub-wavelength inter-distances requires new communication models that account, at the optimization stage, for the mutual coupling among the elements [17], [18], [19], [20].

9.1.2 Electromagnetically consistent modeling of reconfigurable intelligent surfaces

In this chapter, we focus our attention on RISs. The deployment and optimization of RISs in wireless networks need several challenges to be tackled. Interested readers can consult, e.g., [5], [8] for a comprehensive discussion. One of the major and open research challenges in RIS-aided wireless communications lies in developing and utilizing electromagnetically-consistent models that account for the practical implementation of RISs. A comprehensive summary of the communication models most widely utilized in wireless communications for RISs is reported in [21]. From the overview in [21], it is apparent that three main communication models are typically utilized:

1. The locally periodic discrete model;
2. The mutually coupled antenna-elements model;
3. The inhomogeneous sheets of surface impedance model.

Interested readers are referred to [21] for a comprehensive discussion of the main characteristics, strengths, and limitations of these models. In this contribution, we focus our attention on the **locally periodic discrete model**, since it is the most widely used model in wireless communications and in the field of **digital metasurfaces** [22]. According to this model, an RIS is modeled as an ensemble of reconfigurable elements, which can be configured in a finite number of states. From an implementation standpoint, each RIS reconfigurable element is made of one or several engineered scattering elements and some electronic circuits. From a signal and system (or communication) standpoint, each RIS reconfigurable element is associated with a discrete-valued alphabet, sometimes referred to as lookup table or codebook, which determines the finite number of

has been measured for the broadside beam (the one more degraded by the presence of the WAIM), resulting in a maximum IL in-band of 0.2 dB to 0.4 dB.

11.3 Two sectors cell coverage for costs reduction

Traditional base station sites, both in legacy and in new 5G systems, typically employ a three-antenna configuration in a triangular arrangement, so that each antenna is demanded to provide coverage over a 120° angular sector. By skillfully combining the overlapping regions at the border of each antenna coverage sector, full 360° cell coverage is achieved. Even in the dynamic, reconfigurable beam environment of novel 5G systems, the azimuth scanning capability of a traditional phased array, with canonical horizontal elements spacing at or close to half a wavelength to avoid in-sector grating lobes, is limited to 120°. This limitation originates from two main factors:

- the loss of gain caused by reduction in the size of the array aperture when projected along the beam pointing direction;
- the active return loss degradation caused by the surface currents induced on the array surface when the beam is steered in directions close to the end-fire.

In certain scenarios, such as scarcely populated or rural areas, it makes sense, from a commercial point of view, to try to limit the ownership cost of the site by trying to reduce the cost of the installed hardware (capital expenditure, CAPEX) and the operational expenditure (OPEX) by reducing the power consumption of the overall site. A method to achieve this result is to try to overcome the scanning limitations of the array and to extend azimuth scanning from +/-60° to +/-90° by placing a divergent lens in front of the phased array, even accepting to pay the price of slightly reduced antenna performance. The enhanced scanning capabilities provided by the lens make cell coverage possible by placing two antenna systems in a back-to-back configuration, instead of the usual three, allowing for a considerable reduction of the site's ownership cost. Fig. 11.7 presents the traditional three sectors approach against the proposed two sectors configuration exploiting enhanced array scanning range.

Traditional lenses are made by either properly shaping the profile of a controlled dielectric material or by locally changing the dielectric constant by mechanically removing material, therefore creating a local dielectric constant, which effectively is the weighted average of the material's dielectric constant and the vacuum's. Since both of these approaches are based

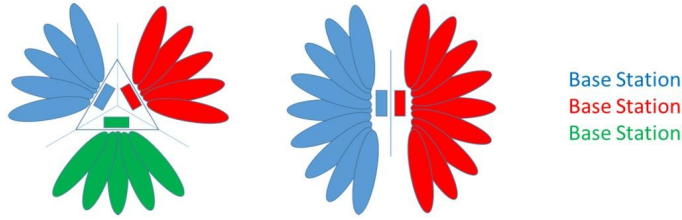

Figure 11.7 3-sectors cell coverage vs 2-sectors cell coverage.

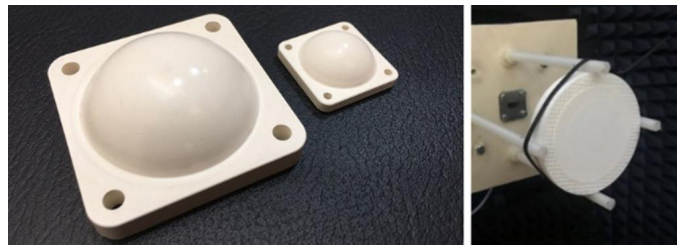

Figure 11.8 A dielectric lens made using PREPERM dielectric materials. Picture courtesy of Avient (left), graded index lens (right) [32].

mostly either on *geometrical optics* or *ray tracing* approach, analytical equations can be derived for the synthesis of these lenses [31]. This type of solution, though effective from the electromagnetic point of view, is often not convenient as it requires bulky structures made of high quality, low loss and expensive dielectric material to be assembled in front of the antenna. Fig. 11.8 shows an example of both a dielectric lens and a graded index (GRIN) lens.

11.3.1 Two-sector deployment: metaradome as MTS-based implementation

A metasurface-based lens (metalens) represents a valid alternative to bulky and expensive dielectric or GRIN lenses. The divergence of a traditional lens can be replicated with a metalens by properly designing the phase profile of the collection of metacells forming the metasurface in such a way as to provide minimal defocusing effect when most of the radiated energy is impinging the central section of the metalens, while providing an increasingly larger deflection when the energy is impinging on either side of the metalens. Clearly, the individual cells must also be designed to maximize the value of the transmission coefficient, to minimize the loss of *gain*